

Multipass cell design for Stark-modulation spectroscopy

Christoph Dyroff,^{1,*} Andreas Zahn,¹ Wolfgang Freude,² Bernd Jänker,³ and Peter Werle^{1,4}

¹Research Center Karlsruhe, Institute for Meteorology and Climate Research, Hermann-von-Helmholtz-Platz 1, 76344 Eggenstein-Leopoldshafen, Germany

²Institute of High-Frequency and Quantum Electronics, Universität Karlsruhe (TH), Engesserstrasse 5, 76131 Karlsruhe, Germany

³Carl Zeiss SMT AG, Carl Zeiss Strasse 22, 73447 Oberkochen, Germany

⁴CNR-National Institute for Applied Optics, Largo Enrico Fermi, 6, 50125 Florence, Italy

*Corresponding author: christoph.dyroff@imk.fzk.de

Received 29 September 2006; revised 2 February 2007; accepted 12 February 2007;
posted 13 February 2007 (Doc. ID 75614); published 12 June 2007

A multipass cell for absorption measurements with an additionally applied homogeneous electric field for Stark effect measurements is described. The configuration is based on two ring mirrors, where the laser beam propagates between two nested cylindrical-wall electrodes. The total optical path length achieved is 40 m. The beam pointing stability of this setup is investigated and compared to a confocal-type Herriott cell of the same base length, employing numerical simulations. The exit beam pointing stability is found to be very good. The response measurements show fast exchange times, which agree well with theoretical values. © 2007 Optical Society of America

OCIS codes: 120.6200, 260.6580, 300.6380, 300.1030.

1. Introduction

Modulation spectroscopy is a well-established technique to detect trace amounts of molecular species. It is based on a single narrow laser line being tuned over an absorption line of interest while periodically modulating the laser wavelength. The detector signal is then demodulated using a lock-in amplifier at either the modulation frequency or twice the modulation frequency to record first- or second-derivative spectra. The target gas is commonly pumped through an absorption cell at reduced pressure to increase selectivity and signal by reducing the absorption linewidth. To further increase the absorption signal and lower the detection limit, long path-length multipass absorption cells are used. In these cells the laser beam is reflected back and forth between two mirrors (Herriott-type) [1–4] or three mirrors (White-type) [5–7]. However, owing to scattering at the mirrors' reflective surfaces a fraction of the laser radiation may interfere with the laser beam, and, when traveling in the laser beam direction, may ultimately hit the detector. When recording spectra, a superimposed etalon

structure is observed having a fringe period corresponding to the absorption cell base length, i.e., for a cell of 0.5 m base length the fringe period is approximately 300 MHz. Additional etalon structures may arise from other sources, such as reflections from optical elements such as lenses. While high-frequency etalon structures may be eliminated by numerical or electronic means, this is not easily accomplished for structures with frequencies close to the width of the absorption line of interest. Since absorption spectroscopy is often performed at reduced pressure to increase selectivity, the linewidth is close to the fringe period estimated above.

Then the standard technique to suppress the etalon structures from the spectra is to switch between ambient (target gas) and background (zero air) signals, and subsequently subtract the background signal from the ambient signal. However, the background signal is generally time dependent, and after a certain time the subtraction of an old background will result in erroneous data. The maximum time for background subtraction (stability time) can be well determined by the Allan variance method introduced by Werle *et al.* [8]. This method has become a standard procedure in diode laser spectroscopy to characterize system stability and drift, which is the major limitation in the

measurements [9–15]. By proper design and thermal stabilization, stability times of several tens of seconds up to 260 s have been achieved [15]. However, new solutions have to be found for longer stability times to allow integration over longer time periods, either to improve the detection limit to optical densities beyond the lower 10^{-7} range, or to increase the signal-to-noise ratio for an increased measurement precision [16].

As reported (for formaldehyde) by Werle and Lechner [17] a Stark modulation of the absorption line of interest, as an addition to wavelength or frequency modulation spectroscopy, can be used to overcome this limitation. This technique is based on the splitting and the shift of the rotational–vibrational energy levels (i.e., ground and excited state) of an absorption transition when applying an external electric field to the sample species of interest. Using a periodically changing electric field it is thus possible to modulate the absorption signal for a given laser wavelength by periodically shifting the absorption line with respect to the laser line. In this case the background etalon structures are not affected by the electric field, and by demodulating the detector signal with a lock-in am-

plifier it is thus possible to separate the signal of the absorption line and that of the etalon background.

Thus far, the technique has been demonstrated with a single path absorption cell with a 35 cm optical path length [17]. For field measurements, path lengths of several tens of meters are required for low concentration measurements. In the present paper the design of a multipass absorption cell for Stark-modulation enhanced absorption spectroscopy is presented, which provides an up to 100 times larger optical path length than a previous demonstration experiment [17]. Calculated and measured optical patterns are compared, and misalignment effects that may occur during the operation of the cell are quantified. Finally, absorption measurements for checking the time response of the cell to a gas concentration step function for polar molecules (H_2O) are discussed.

2. Cell Design Considerations

The optical part of a multipass cell in general consists of two mirrors located vis-à-vis on an optical axis as indicated in Fig. 1(a). Light is repeatedly reflected

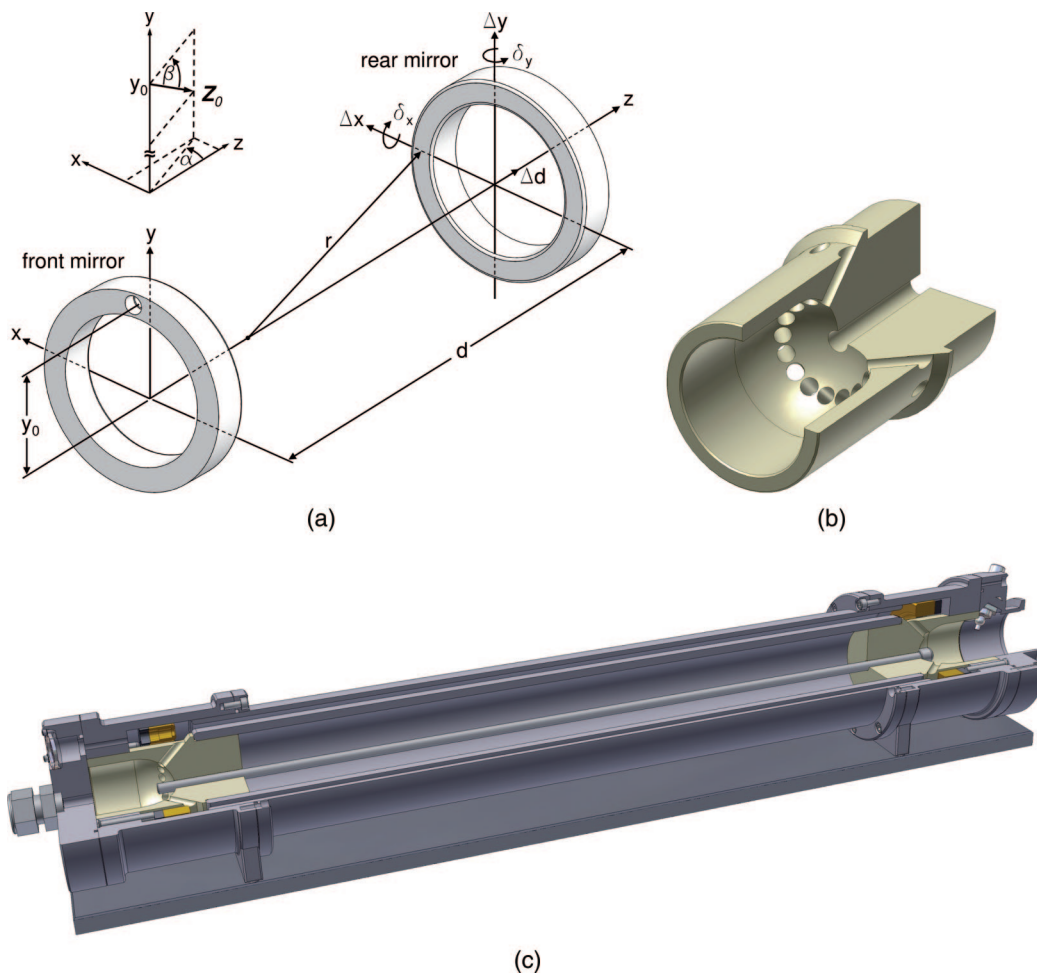


Fig. 1. (a) Multipass cell mirrors with radius r , spaced by distance d . The coupling hole is located in the front mirror at x_0 and y_0 . The cell axis coincides with the z axis. (b) Section view of the ceramic flow-inlet part of the cell. The ceramic also provides proper electrical isolation against the inner electrode. (c) Rendered cross section of the cell showing the two nested cylindrical electrodes.

between either spherical mirrors as proposed by Herriott *et al.* [1] or astigmatic mirrors as in an approach by McManus *et al.* [3]. The latter design allows reaching higher path lengths at a small volume and simultaneously optimizes the separation of subsequent spots on the two mirrors for minimizing the etalon effect. In the classical configuration, the spots on the mirrors form an ellipse, whereas in the latter configuration the spots form a Lissajous pattern originating from the astigmatism of the mirrors. In both cases the laser beam is injected into the cell through a coupling hole in the front mirror at a certain angle with respect to the cell axis (z axis). The beam leaves the cell through the same coupling hole under the same, but inverted angle.

The cell contains two gold-coated spherical ring mirrors of 74 mm diameter and a focal length of $f = 5500$ mm. A coupling hole of 4.5 mm diameter is located in the front mirror at a position $y_0 = 32.5$ mm from the cell axis. Each mirror is mounted by three spring-loaded screws in a stainless-steel housing. The front housing contains a CaF_2 window for beam entrance and exit. Both housings are connected by a stainless-steel cylinder. A second stainless-steel cylinder is concentrically mounted inside the cell. The nested cylindrical electrodes confine the gas sample volume and also form the electrodes for electric field application [Fig. 1(c)]. Gas flow connectors are located at both housings. The spacing of the electrodes should be as small as possible (a few millimeters to 1 cm) to allow for a reasonable field strength of the order of ~ 1 kV/cm. Such a parallel electrode arrangement prevents the use of a confocal multipass cell approach, i.e., a design where the mirror radius of curvature r corresponds to the separation of the mirrors d , because the beam path frequently crosses the cell center and is not limited to a cylindrical shell. Therefore the usual mirror arrangement of Herriott cells cannot be combined with the Stark sample modulation technique. In the following section a novel cell design is presented that allows overcoming this limitation.

The laser beam propagation within the multipass cell is calculated using the equations by Herriott *et al.* [1]. The front and rear mirrors are separated by the distance d , the radius of curvature of the cell mirrors is r , and their focal length is $f = r/2$ [Fig. 1(a)]. The laser beam is coupled into the cell through the coupling hole located in the front mirror at x_0 and y_0 . After entering the cell in an appropriate off-axis direction at angles α and β , the laser beam is reflected back and forth between both mirrors. After n passes the beam hits a mirror at the position x_n, y_n . By a proper choice of the mirror distance d the beam exits the cell after a selected number of passes. Spots with even numbers n lie on the front mirror, spots with odd numbers lie on the rear mirror. Projecting the spots on a single plane leads to the radial-angular displacement θ of two consecutive spots $n, n + 1$:

$$\cos(\theta) = 1 - \frac{d}{2f}. \quad (1)$$

Assuming the paraxial approximation according to Herriott *et al.* [1], we obtain

$$x_n = x_0 \cos(n\theta) + \left(\frac{d}{4f-d}\right)^{1/2} [x_0 + 2f \tan(\alpha)] \sin(n\theta). \quad (2)$$

A similar equation holds for the y direction.

If the laser beam leaves the cell after N passes through the cell, M concentric circles on each mirror appear. This is termed the reentrant condition:

$$N\theta = 2\pi M, \quad M = 1, 2, 3, \dots \quad (3)$$

As pointed out by Durry *et al.* [18] the reentrant condition depends only on the mirror separation d and the mirror focal length f , no matter what the entrance angles α, β and the coordinates x_0, y_0 are. The practical constraints are the size of the reflective mirror surface and the shape of the spot pattern, i.e., elliptical or circular. Combining Eqs. (1) and (3) leads to the required mirror separation for a given mirror focal length

$$d = 2f \left[1 - \cos\left(2\pi \frac{M}{N}\right) \right]. \quad (4)$$

There are many combinations of integers N and M that fulfill the reentrant condition in Eq. (3). As the laser beam has to be guided through a rather narrow gap between two cylindrical electrodes the off-axis angle of the beam and hence the angular spot displacement θ [Eq. (1)] have to be small. This leads to a long focal length f , and consequently to a small integer M .

The formalism described above has been used to specify the design parameters of the cell. We chose $N = 86$ and $M = 4$ at $f = 5500$ mm to achieve an approximate optical path length of 40 m at $d = 466.4$ mm. We realize a cylindrical spot pattern by injecting the beam at $\alpha = 1.13^\circ$ and $\beta = -0.19^\circ$, i.e., by pointing the beam onto a circle with 32.5 mm diameter on the rear mirror. The coupling hole is located at $x_0 = 0$ and $y_0 = 32.5$ mm. According to

$$L = \frac{1}{M} \sqrt{(x_n - x_{n+2})^2 + (y_n - y_{n+2})^2}, \quad (5)$$

the distance L between two consecutive spots on the mirror is ~ 4.6 mm for $M = 4$. Such a small spot distance requires small spot sizes, which in turn leads to the required focusing optics. Coupling into the cell is achieved by aiming the laser beam through the coupling hole of the front mirror with a focus at

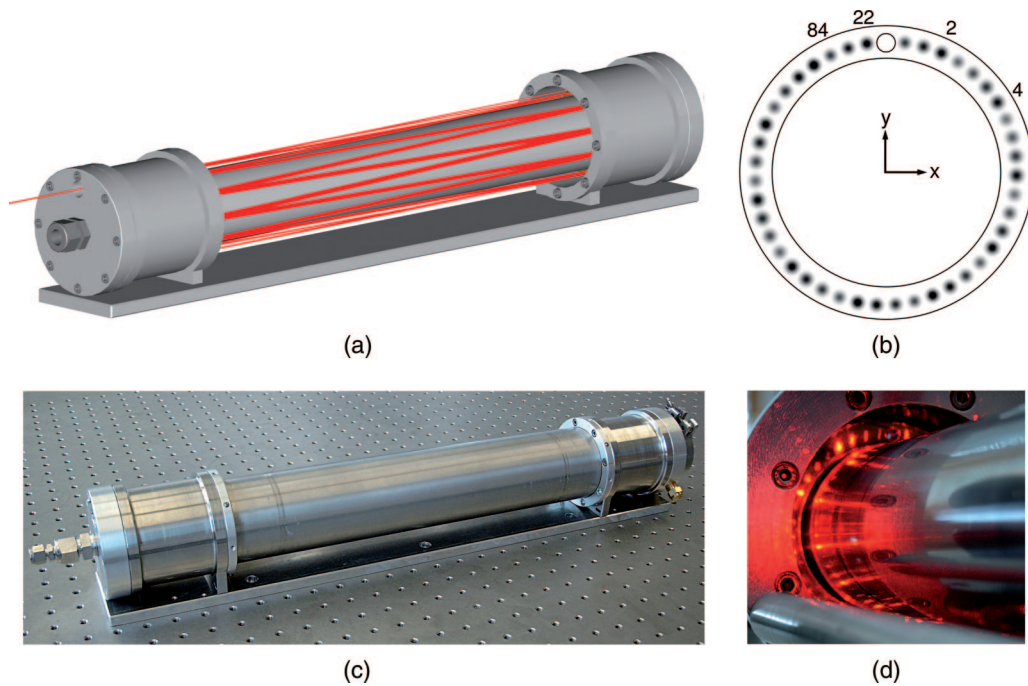


Fig. 2. (a) Ray tracing simulation of the multipass cell for the first 22 passes. The outer electrode has been removed for clarification. (b) Spot pattern on the front mirror as observed from inside the cell as a result of a complete ray tracing simulation. (c) Photograph of the cell. (d) Photograph of the front mirror with the beam of a red trace laser aligned through the cell. The outer electrode has been removed.

half of the distance between the two mirrors. The NA of the beam is chosen such that the wavefront radius of curvature at the mirror surface matches the mirror radius of curvature. Assuming a fundamental-mode Gaussian beam at 1575 cm^{-1} , as was used by Werle and Lechner [17], we find a spot size of $w_0 = 1.7\text{ mm}$ at a NA of $A_N = 1.07 \times 10^{-3}$. A comparison of the calculated beam path and the experimental results is shown in Figs. 2(b) and 2(d).

The misalignment of multipass cells, especially during field measurements attributable to vibrations, accelerations (shocks) and ambient temperature and pressure variations, is known to degrade the performance of tunable diode laser absorption spectrometers considerably [19,20]. Subtle alignment changes can dramatically affect the retrieved trace gas concentrations, mainly because of changing spectral background structures. In the following, we estimate the effect of alignment instabilities, *inter alia*, to quantify the tolerances during cell alignment. We consider misalignment errors that are caused by (a) changes in mirror separation Δd , (b) transverse mirror displacements Δx and Δy , and (c) tilt of the mirrors δ_x and δ_y [Fig. 1(a)]. To quantify these misalignment errors we use an *ABCD* matrix description of the cell optics.

In an ideal centered collinear optical system, we can use a 2×2 ray-transfer matrix to represent the transformation of a ray between two reference planes (RP) according to the matrix equation

$$\begin{bmatrix} x_1 \\ \tan(\alpha_1) \end{bmatrix} = \begin{bmatrix} A & B \\ C & D \end{bmatrix} \begin{bmatrix} x_0 \\ \tan(\alpha_0) \end{bmatrix}, \quad (6)$$

where x_0 and $\tan(\alpha_0)$ are the components of the incident ray vector, denoting the position of the ray and its slope with respect to the optical axis, respectively. This is illustrated in Fig. 3 for an arbitrary transformation matrix with elements *A*, *B*, *C*, and *D*, where both reference planes are located at the same position on the optical axis (RP). Applying the transformation matrix to the incident ray vector yields the resulting position and slope x_1 and $\tan(\alpha_1)$ after the optical element described by the transformation matrix.

In an actual system the position of the optical axis in the second reference plane may be displaced slightly from its assumed position by a small distance Δx . Also, the direction in which the optical axis is pointing may deviate slightly by a small amount δ_x . We can represent this misalignment by adding misalignment terms to Eq. (6), and Gerrard and Burch [21] suggest adding a third dummy equation,

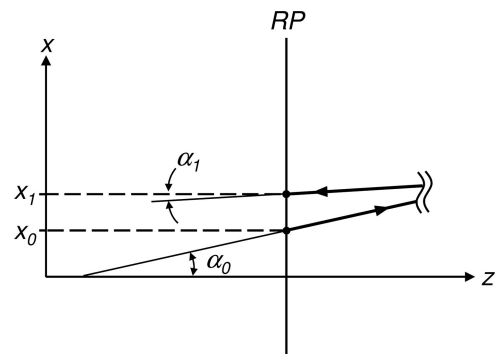


Fig. 3. Propagation of a ray vector between two coincident RPs.

$$\begin{aligned}
x_1 &= Ax_0 + B \tan(\alpha_0) + \Delta x, \\
\tan(\alpha_1) &= Cx_0 + D \tan(\alpha_0) + \delta_x, \\
1 &= 0 + 0 + 1.
\end{aligned} \tag{7}$$

These equations can again be written in matrix form

$$\begin{bmatrix} x_1 \\ \tan(\alpha_1) \\ 1 \end{bmatrix} = \begin{bmatrix} A & B & \Delta x \\ C & D & \delta_x \\ 0 & 0 & 1 \end{bmatrix} \begin{bmatrix} x_0 \\ \tan(\alpha_0) \\ 1 \end{bmatrix}. \tag{8}$$

In the description of the multipass cell optics the 3×3 matrix in Eq. (8) denotes the reflection matrix \mathbf{R}_x :

$$\mathbf{R}_x = \begin{bmatrix} 1 & 0 & \Delta x \\ -2/r & 1 & \delta_x \\ 0 & 0 & 1 \end{bmatrix}, \tag{9}$$

where r is the radius of curvature of the mirror, Δx is a small transverse displacement of the mirror axis, and δ_x is a small tilt of the mirror axis with respect to the optical axis. \mathbf{R}_x describes the reflection in the zx plane and a similar quantity \mathbf{R}_y is valid in the yz plane.

The actual optical system of the multipass cell contains two different matrices, the reflection matrix \mathbf{R}_x of each of the two mirrors and a matrix \mathbf{D}_x of a plane-parallel plate of air, which separates the reference planes of both mirrors,

$$\mathbf{D}_x = \begin{bmatrix} 1 & d + \Delta d & 0 \\ 0 & 1 & 0 \\ 0 & 0 & 1 \end{bmatrix}. \tag{10}$$

The term Δd accounts for changes in the separation of the two multipass cell mirrors. The matrix for a single pass through the cell, e.g., from the coupling hole to the rear mirror, is calculated by $\mathbf{M}_x = \mathbf{R}_x \mathbf{D}_x$. The ray starts at the first reference plane of the front mirror. It then passes through the plane-parallel plate of air (\mathbf{D}_x) and is reflected by the rear mirror (\mathbf{R}_x). The second reference plane refers to the rear mirror. To calculate the position of the beam on the mirrors after n passes, \mathbf{M}_x is raised to the power of n and multiplied by the incident ray vector at the first reference plane $\mathbf{Z}_0 = \{x_0; \tan(\alpha_0); 1\}^T$:

$$\mathbf{Z}_n|_x = \mathbf{M}_x^n \mathbf{Z}_0. \tag{11}$$

An equivalent formulation is valid for the y direction. Together, $\mathbf{Z}_n|_x$ and $\mathbf{Z}_n|_y$ form the ray vector \mathbf{Z}_n that contains the coordinates x_n, y_n and the slopes $\tan(\alpha_n), \tan(\beta_n)$ of the ray at the n th reference plane. Here $\tan(\beta_n)$ denotes the slope of the ray in the yz plane after n passes. Again, spots with even numbers n lie on the front mirror, spots with odd numbers n lie on the rear mirror. Based on the formalism described

above the misalignment of \mathbf{Z}_n has been calculated and compared with that of a confocal Herriott cell with approximately the same mirror separation and a circular spot pattern of equivalent diameter while introducing the three sources of misalignment listed above. We note that the matrix description discussed above describes only the propagation of the center ray and does not fully describe the propagation of a practical laser beam. Furthermore, we assume a paraxial approximation and neglect higher-order effects. The results are based on coupling into the cell in a way to obtain a circular spot pattern, which is a prerequisite for our design. Changes in the angles α and β would lead to slightly different results [compare with Eq. (2)].

Changes of mirror distance Δd are usually related to thermal drifts of the cell or pressure changes inside or outside the cell (e.g., for an airborne instrument during ascent or descent of the aircraft). The coefficient of thermal expansion of stainless steel is $16 \times 10^{-6} \text{ K}^{-1}$ at 20°C [22], and the base length of our cell is $d = 466.4 \text{ mm}$. An assumed temperature increase of the cell by 2 K leads to an increase in base length of $\Delta d = 15 \text{ }\mu\text{m}$. Our calculations demonstrate that the ray at the coupling hole after $N = 86$ passes is displaced by only $13.5 \text{ }\mu\text{m}$ along the x direction. This corresponds to a ratio of $\Delta x/\Delta d = 0.9$. The beam pointing angle α_n changes by $\Delta\alpha_n/\Delta d = 4.5 \times 10^{-3} \text{ deg/mm}$. The beam displacement in the y direction (Δy) is negligible ($\Delta y/\Delta d < 0.02$), whereas the beam pointing angle β_n changes at a ratio of $\Delta\beta_n/\Delta d = 3.1 \times 10^{-2} \text{ deg/mm}$. With a misalignment of $\Delta d = 15 \text{ }\mu\text{m}$ we find for the confocal cell that the beam is displaced in the x direction by $81 \text{ }\mu\text{m}$ ($\Delta x/\Delta d = 5.4$) with $\Delta\alpha_n/\Delta d = 0.61 \text{ deg/mm}$. In the y direction we calculate a displacement of $7.2 \text{ }\mu\text{m}$ ($\Delta y/\Delta d = 0.48$), whereas the beam pointing angle changes by $\Delta\beta_n/\Delta d = 0.66 \text{ deg/mm}$. The calculated ratios are linear approximations that are valid for small changes Δd . For a better comparison of the cell characteristics the data are summarized in Table 1.

Maximum transverse mirror displacements and mirror tilt put constraints on construction tolerances and accuracy of alignment. The calculations show that both position and pointing angles do not change with transverse mirror displacement and/or

Table 1. Comparison of Beam Displacement $\Delta x, \Delta y$ and Beam Pointing Angle $\Delta\alpha_n, \Delta\beta_n$ Due to Changes in Mirror Separation Δd for the Present Stark-Modulation Cell and a Confocal Herriott Cell with a Circular Spot Pattern of the Same Diameter^a

	Stark-Modulation Cell	Herriott Cell
Volume	0.81	~21
Path length	40 m	40 m
$\Delta x/\Delta d$	0.9	5.4
$\Delta y/\Delta d$	~0	0.48
$\Delta\alpha_n/\Delta d$	$4.5 \times 10^{-3} \text{ deg/mm}$	0.61 deg/mm
$\Delta\beta_n/\Delta d$	$3.1 \times 10^{-2} \text{ deg/mm}$	0.66 deg/mm

^aThe ratios are linear approximations, which are valid for small changes Δd .

mirror tilt. This holds true for the confocal arrangement as well. The spot pattern becomes distorted, i.e., elliptical. The level of ellipticity is very similar for the confocal and nonconfocal configuration when displacing one or both mirrors transversally. However, introducing mirror tilt reveals much less ellipticity of the pattern for the confocal arrangement. Therefore the initial alignment of the Stark multipass cell is more demanding than that of a classical confocal Herriott cell.

3. High Voltage, Gas Flow, and Exchange Rate Aspects

For Stark sample modulation, the two concentrically aligned cylinders form the electrodes for the application of the electric field. The gap between the electrodes is 7.75 mm. The surfaces facing each other are highly polished and the edges are rounded to avoid sparking. The inner electrode is connected to the high electric potential, while the outer electrode as well as the rest of the cell housing is connected to ground potential. The threshold electric field E_{th} , above which sparking occurs, depends on the gas between the electrodes, its pressure p , and the electrode gap g . It is defined by the Paschen law [23]

$$E_{th} = \frac{ag}{\ln(pg) + b}. \quad (12)$$

The factors a and b are tabulated values for the specific gas between the electrodes (we used $a = 273.8 \text{ V}/(\text{cm} \times \text{hPa})$ and $b = 0.89 \text{ l}/(\text{cm} \times \text{hPa})$ for air) [23]. Figure 4 shows the theoretical Paschen curve based on Eq. (12) along with the measured values. The measurement reveals a slightly lower threshold electric field than theory predicts. This can be attributable to inhomogeneities of the electric field, causing sparking at electric fields lower than theory predicts. The measured data are also shifted to a lower pg , which can be assigned to a mismatch

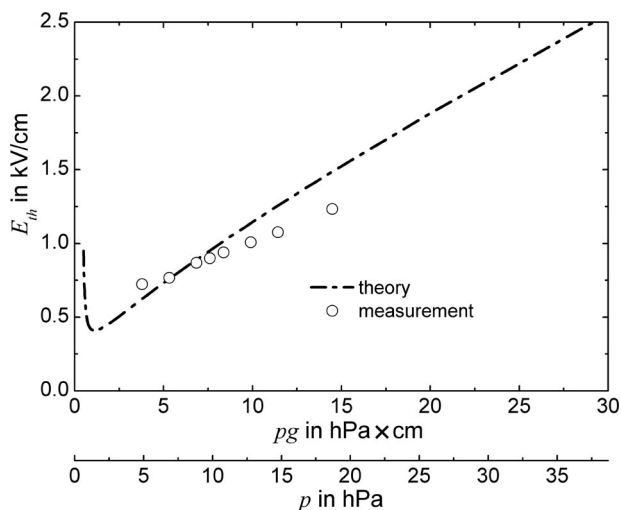


Fig. 4. Threshold electric field E_{th} versus pressure-gap-product pg in air [23]. The electrode gap for the measurement was 7.75 mm.

between measured and actual pressure, as the pressure was measured downstream of the cell. The number of measurements was limited by the maximum voltage of 1000 V ($E = 1290 \text{ V}/\text{cm}$) achievable by our high voltage supply.

The lower threshold electric field measured is generally no limitation for the intended application of this cell, i.e., wavelength modulation spectroscopy in conjunction with sample modulation based on the Stark effect [17]. For wavelength modulation spectroscopy in the mid-IR spectral region, the maximum signal is achieved at pressures of approximately 20–50 hPa. For example, the CH_2O doublet at 1757.94 cm^{-1} investigated by Werle and Lechner [17], which will be used in further studies employing the present cell (see Section 4), showed a maximum signal at a cell pressure of 25 hPa.

The inner electrode is fitted with ceramic end pieces [Fig. 1(b)] to ensure the electrical isolation of the mirror housings. The end pieces are designed such that the gas flow is evenly distributed into the sample volume, while the cross-sectional area within the end pieces matches that of the sample volume, thus enabling a laminar flow. This is important for two reasons. First, the turbulent motion of the sample gas leads to small local variations in temperature and pressure, which in turn produce local refractive index variations. These refractive index fluctuations may have a slightly higher or lower refractive index, and can be thought of as an eddy, which may behave the same way as a lens [24]. While the laser beam propagates through a large number of refractive index inhomogeneities, the cumulative effect can be very significant and produce optical phase effects, which in turn lead to angle-of-arrival fluctuations or beam wander, intensity fluctuations, and beam broadening. Second, a homogeneous flow in the cell leads to a fast cell response time because of a minimization of recirculation zones that would increase the response time of the cell [3]. Fast cell response is important for high sampling rates, e.g., for eddy correlation flux measurements.

The measurements of the gas exchange rate for a polar molecule were carried out by alternately injecting ambient air (approximately 30% relative humidity) and dry nitrogen (grade 6.0, $[\text{H}_2\text{O}] < 0.5 \text{ ppmv}$) into the cell and then measuring the optical absorption of an H_2O absorption line at 7182.209 cm^{-1} [Fig. 5(a)]. The gas was injected with a rectangular time dependence as shown in Fig. 5(b) by rapidly switching between the two gases. The data acquisition rate of the measurement was 2.5 Hz (0.4 s). The cell pressure and flow rate were 140 hPa and 4.75 L/min ($1\text{L} = 1000 \text{ cm}^3$ at 1013 hPa and 0°C), respectively. The measurement was performed at room temperature.

A single exponential fit was used to deduce the time constant ($1/e$ time) of the rising edges of the cell response. For the falling edges a second-order exponential fit was used to account for gas exchange as well as H_2O desorption off the cell walls. The fit re-

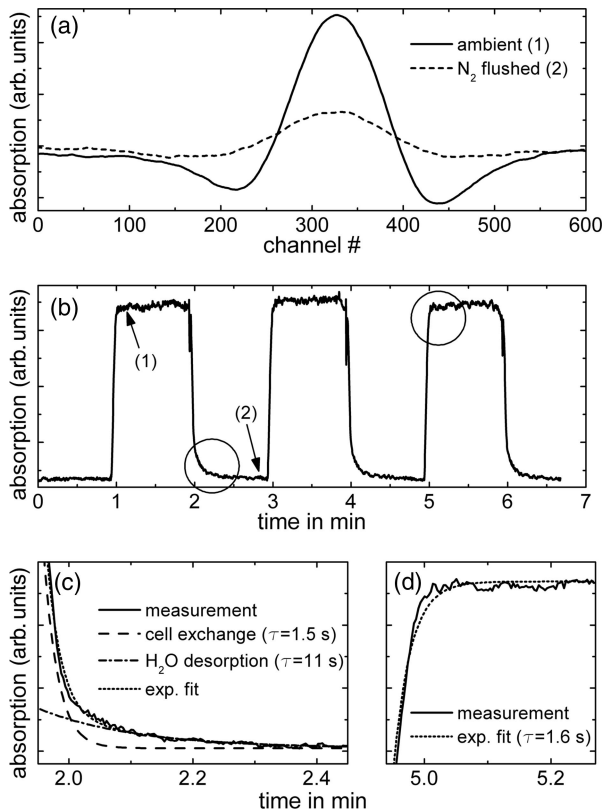


Fig. 5. (a) Second-derivative spectra of H₂O at approximately 7182.209 cm⁻¹ for ambient H₂O (solid curve) and residual H₂O (dashed curve), when the cell was flushed with dry nitrogen. (b) Response of the cell to a square wave of ambient H₂O at a pumping speed of 4.75 L/min. (c) Gas exchange time at the falling edge is 1.5 s. A second long time constant of 11 s is attributable to water desorption off the cell and upstream tubing walls. (d) Gas exchange time at the rising edge is 1.6 s.

veals a gas exchange time of approximately 1.5 s, corresponding very well to the cell and upstream tubing volume of approximately 0.85 l. The time constant for the H₂O desorption was approximately 11 s. As the measurement was performed at room temperature, this time constant can be significantly reduced by heating the cell.

4. Summary and Conclusions

Field laser applications in industry and research require instruments capable of quantifying small concentrations of trace gases. Meanwhile, diode-laser spectroscopy is a well-established technique for such measurements. The most important application of tunable diode lasers is their use in conjunction with a long-path cell to provide high-sensitivity local measurements. Modulation techniques allow us to detect absorptions below 10⁻⁶ for integration times of approximately 1 s. This sensitivity combined with an optical path length of several tens of meters, translates into parts per billion by volume to parts per trillion by volume detection limits. When the wavelength of the diode laser is tuned over an absorption line, a periodic, often nonstationary fringe structure is superimposed on the desired signal of the absorp-

tion of the target gas, which is frequently called the etalon effect. These fringes are generated inside optical resonators between surfaces of windows, lenses, and even the laser and the detector crystal. For spectroscopic techniques, the problem of fringe reduction is key to improving sensitivity. For reaching the quantum limit several approaches use advanced designs and measurement techniques [25], but they do not solve the problem of baseline drift. Therefore the problem of baseline drifts remains an important issue for the design of ultrasensitive spectrometers for laboratory use as well as for operational instrumentation for field measurements. An effective fringe reduction technique can be obtained through an additional selective modulation of the spectral feature under investigation, which does not affect fringes and background structure.

We have described the design of a novel multipass cell, which allows the application of a sample modulation based on the Stark effect. The multipass cell consists of two spherical ring mirrors with radius of curvature and displacement chosen such that an optical path length of 40 m as a result of 86 passes through the cell is achieved. Two nested metal cylinders form the electrodes of the application of an electric field of up to 1 kV/cm and confine the sample gas in an overall volume of only 0.85 l, which is advantageous for fast measurements. The first experimental flow response tests with a NIR diode laser show that the gas exchange rate is in good agreement with the active cell volume. From the response of the cell to a square wave of ambient H₂O at a pumping speed of 4.75 L/min, the gas exchange time of the falling edge has been determined to be 1.5 s with a second, longer time constant of 11 s attributable to water desorption off the cell and upstream tubing walls. Finally, numerical simulations reveal an improved beam pointing stability compared to a classical confocal Herriott cell.

While generally the cell can be used for all absorption measurements, the Stark-modulation technique is applicable to many molecules with a permanent dipole moment such as formaldehyde, hydrogen peroxide, nitric acid, ammonia, hydrogen chloride, nitrogen dioxide, and nitrous oxide [17]. Therefore as a next step we will investigate the suppression of background fluctuations and the improvement in signal-to-noise ratio, sensitivity, and detection speed in conjunction with mid-infrared lasers, based on the single-path measurements discussed by Werle and Lechner [17].

References

1. D. Herriott, H. Kogelnik, and R. Kompfner, "Off-axis paths in spherical mirror interferometers," *Appl. Opt.* **3**, 523–526 (1964).
2. J. Altmann, R. Baumgart, and C. Weitkamp, "Two-mirror multipass absorption cell," *Appl. Opt.* **20**, 995–999 (1981).
3. J. B. McManus, P. L. Kebabian, and M. S. Zahniser, "Astigmatic mirror multipass absorption cells for long-path-length spectroscopy," *Appl. Opt.* **34**, 3336–3348 (1995).
4. J. A. Silver, "Simple dense-pattern optical multipass cells," *Appl. Opt.* **44**, 6545–6556 (2005).

5. J. U. White, "Long optical paths of large aperture," *J. Opt. Soc. Am.* **32**, 285–288 (1942).
6. J.-F. Doussin, R. Dominique, and C. Patrick, "Multiple-pass cell for very-long-path infrared spectrometry," *Appl. Opt.* **38**, 4145–4150 (1999).
7. S. M. Chernin and E. G. Barskaya, "Optical multipass matrix systems," *Appl. Opt.* **30**, 51–58 (1991).
8. P. Werle, R. Mücke, and F. Slemr, "The limits of signal averaging in atmospheric trace-gas monitoring by tunable diode-laser absorption spectroscopy (TDLAS)," *Appl. Phys. B* **57**, 131–139 (1993).
9. D. G. Lancaster, A. Fried, B. Wert, B. Henry, and F. K. Tittel, "Difference-frequency-based tunable absorption spectrometer for detection of atmospheric formaldehyde," *Appl. Opt.* **39**, 4436–4443 (2000).
10. J. A. Silver and W. R. Wood, "Miniature gas sensor for monitoring biological space environments," in *Diode Lasers and Applications in Atmospheric Sensing*, A. Fried, ed., *Proc. SPIE* **4817**, 82–87 (2002).
11. D. R. Bowling, S. D. Sargent, B. D. Tanner, and J. R. Ehleringer, "Tunable diode-laser absorption spectroscopy for stable isotope studies of ecosystem-atmosphere CO₂ exchange," *Agric. Forest Meteorol.* **118**, 1–19 (2003).
12. D. D. Nelson, B. McManus, S. Urbanski, S. Herndon, and M. S. Zahniser, "High precision measurements of atmospheric nitrous oxide and methane using thermoelectrically cooled mid-infrared quantum cascade lasers and detectors," *Spectrochim. Acta Part A* **60**, 3325–3335 (2004).
13. P. Werle, P. Mazzinghi, F. D'Amato, M. De Rosa, K. Maurer, and F. Slemr, "Signal processing and calibration procedures for *in situ* diode-laser absorption spectroscopy," *Spectrochim. Acta Part A* **60**, 1685–1705 (2004).
14. S. R. Saleska, J. H. Shorter, S. Herndon, R. Jiménez, J. B. McManus, J. William Munger, D. D. Nelson, and M. S. Zahniser, "What are the instrumentation requirements for measuring the isotopic composition of net ecosystem exchange of CO₂ using eddy covariance methods?" *Isotopes Environ. Health Stud.* **42**, 115–133 (2006).
15. P. Weibring, D. Richter, A. Fried, J. G. Walega, and C. Dyroff, "Ultra-high-precision mid-IR spectrometer II: system description and spectroscopic performance," *Appl. Phys. B* **85**, 207–218 (2006).
16. P. Werle, C. Dyroff, A. Zahn, P. Mazzinghi, and F. D'Amato, "A new concept for sensitive *in situ* stable isotope ratio infrared spectroscopy based on sample modulation," *Isotopes Environ. Health Stud.* **41**, 323–333 (2005).
17. P. Werle and S. Lechner, "Stark-modulation-enhanced FM-spectroscopy," *Spectrochim. Acta Part A* **55**, 1941–1955 (1999).
18. G. Durray, T. Danguy, and I. Pouchet, "Open multipass absorption cell for *in situ* monitoring of stratospheric trace gas with telecommunication laser diodes," *Appl. Opt.* **41**, 424–433 (2002).
19. C. Dyroff, D. Richter, A. Fried, J. G. Walega, M. S. Zahniser, and J. B. McManus, "Design and performance assessment of a stable astigmatic Herriott cell for trace gas measurements on airborne platforms," in *Laser Applications to Chemical and Environmental Analysis* (Annapolis, 2004).
20. C. Roller, A. Fried, J. Walega, P. Weibring, and F. Tittel, "Advances in hardware, system diagnostics software, and acquisition procedures for high performance airborne tunable diode laser measurements of formaldehyde," *Appl. Phys. B* **82**, 247–264 (2005).
21. A. Gerrard and J. M. Burch, *Introduction to Matrix Methods in Optics* (Dover, 1994).
22. H. Kuchling, *Taschenbuch der Physik* (Verlag Harri Deutsch, 1984).
23. Y. P. Raizer, *Gas Discharge Physics* (Springer Verlag, 1991).
24. P. Werle and B. Jänker, "High-frequency-modulation spectroscopy: phase noise and refractive index fluctuations in optical multipass cells," *Opt. Eng.* **35**, 2051–2057 (1996).
25. J. Ye, L. S. Ma, and J. L. Hall, "Ultrasensitive detections in atomic and molecular physics: demonstration in molecular overtone spectroscopy," *J. Opt. Soc. Am. B* **15**, 6–14 (1998).